RSC Advances

Supplementary Information

Facile, ethylene glycol-promoted microwave-assisted solvothermal synthesis of high-performance $LiCoPO_4$ as a high-voltage cathode material for lithium-ion batteries

Jennifer Ludwig,[a] Cyril Marino,[b‡] Dominik Haering,[b] Christoph Stinner,[c] Dennis Nordlund,[d] Marca M. Doeff,[e] Hubert A. Gasteiger[b] and Tom Nilges[a]*

[a] *Technical University of Munich, Department of Chemistry, Synthesis and Characterization of Innovative Materials, Lichtenbergstr. 4, 85747 Garching, Germany*
[b] *Technical University of Munich, Department of Chemistry, Technical Electrochemistry, Lichtenbergstr. 4, 85747 Garching, Germany*
[c] *BMW AG, Petuelring 130, 80788 München, Germany*
[d] *Stanford Synchrotron Radiation Lightsource, SLAC National Accelerator Laboratory, 2575 Sand Hill Rd, Menlo Park, CA, 94025, USA*
[e] *Lawrence Berkeley National Laboratory, Environmental Energy Technologies Division, 1 Cyclotron Rd, Berkeley, CA, 94720, USA*
‡ Present address: *Paul Scherrer Institute, Electrochemical Energy Storage, 5232 Villigen PSI, Switzerland*
* E-Mail: tom.nilges@lrz.tu-muenchen.de

1 State of the art

Table S1 State of the art in the (a) hydrothermal (HT), (b) solvothermal (ST), (c) supercritical fluid (SCF), (d) microwave-assisted hydrothermal (MWHT), and (e) microwave-assisted solvothermal (MWST) synthesis of $LiCoPO_4$[a,b]

Ref.	Material	Reactants	Solvent *T* *t*	Morphology (particle size)	Remarks on synthesis	Cell type	Electrode composition	Electrolyte	C rate (remarks)	Discharge capacity, 1st cycle
a) Hydrothermal (HT) synthesis										
1	LCP	$LiOH \cdot H_2O$ $Co(CH_3COO)_2 \cdot 4\,H_2O$ $(NH_4)_2HPO_4$	H_2O 220 °C 5 h	agglomerates (10–45 μm) of prisms (1 μm × 1 μm × 2 μm)	–	–[c]	50:45:5 wt% (LCP:–[c]:–[c])	1 M $LiPF_6$ in EC/DMC = 1:1 (v/v)	0.1 C	15 mAh/g
1	LCP	$LiOH \cdot H_2O$ $Co(CH_3COO)_2 \cdot 4\,H_2O$ $(NH_4)_2HPO_4$	H_2O 300 °C 5 h	rods (300–700 nm × 5 μm)	PVP dispersant	–[c]	50:45:5 wt% (LCP:–[c]:–[c])	1 M $LiPF_6$ in EC/DMC = 1:1 (v/v)	0.1 C	65 mAh/g
2	LCP/C	Li_3PO_4 $CoSO_4 \cdot 7\,H_2O$	H_2O 200 °C 3 h	agglomerates (< 20 μm) of irregular particles (200–500 nm)	C-coating (CMC) post-annealing (700 °C, 1 h, 3% H_2/Ar)	CR2032 coin cell	75:15:10 wt% (LCP/C: Ketjan black: PVDF)	1 M $LiPF_6$ in EC/DEC = 1:1 (v/v)	0.1 C (CCCV)	45 mAh/g
3	LCP/C	$LiOH \cdot H_2O$ $CoSO_4 \cdot 7\,H_2O$ $(NH_4)_3PO_4 \cdot 3\,H_2O$	H_2O 200 °C 8 h	prismatic rods (0.5 × 3 μm)	C-coating (glucose) post-annealing (750 °C, 2 h, Ar)	CR2016 coin cell	70:20:10 wt% (LCP/C: carbon black: PVDF)	1 M $LiPF_6$ in EC/DMC = 1:1 (v/v)	0.1 C	90 mAh/g
4	LCP/C	Li_3PO_4 $CoSO_4 \cdot 7\,H_2O$	H_2O 200 °C 3 h	agglomerates (< 20 μm) of irregular particles (200–500 nm)	C-coating (CMC) post-annealing (700 °C, 1 h, 3% H_2/Ar)	CR2032 coin cell	75:15:10 wt% (LCP/C: Ketjan black: PVDF)	1 M $LiPF_6$ in EC/EMC = 3:7 (v/v)	0.1 C (CCCV)	99 mAh/g
4	LCP/C	Li_3PO_4 $CoCl_2$	H_2O 200 °C 3 h	agglomerates (< 20 μm) of square-like particles (0.5–2 μm)	C-coating (CMC) post-annealing (700 °C, 1 h, 3% H_2/Ar)	CR2032 coin cell	75:15:10 wt% (LCP/C: Ketjan black: PVDF)	1 M $LiPF_6$ in EC/EMC = 3:7 (v/v)	0.1 C (CCCV)	32 mAh/g
b) Solvothermal (ST) synthesis										
3	LCP/C	$LiOH \cdot H_2O$ $CoSO_4 \cdot 7\,H_2O$ $(NH_4)_3PO_4 \cdot 3\,H_2O$	BA/H_2O = 1:1 (v/v) 200 °C 8 h	microspheres (2–3 μm) of nanorods (35–50 nm × 1 μm)	C-coating (glucose) post-annealing (750 °C, 2 h, Ar)	CR2016 coin cell	70:20:10 wt% (LCP/C: carbon black: PVDF)	1 M $LiPF_6$ in EC/DMC = 1:1 (v/v)	0.1 C	133 mAh/g
5	LCP/C	LiCl $Co(NO_3)_2 \cdot 6\,H_2O$ H_3PO_4	EG 200 °C 10 h	agglomerates (2–3 μm) of irregular particles (200 nm)	C-coating (glucose)	CR2032 coin cell	80:10:10 wt% (LCP/C: acetylene black: PVDF)	1 M $LiPF_6$ in EC/DMC = 1:1 (v/v)	0.2 C	108 mAh/g
6, 7	LCP	$LiOH \cdot H_2O$ LiH_2PO_4 $CoSO_4 \cdot 7\,H_2O$	EG/H_2O = 2:1 (v/v) 220 °C 15 h	hexagonal/ octagonal platelets (50–100 nm × 1 μm)	–	Swagelok cell	80:10:10 wt% (LCP: Super P: PVDF)	1 M $LiPF_6$ in EC/DMC = 1:1 (w/w)	0.1 C	95 mAh/g
8	LCP/C	Li_3PO_4 $CoSO_4 \cdot 7\,H_2O$	EG/H_2O = 4:1 (v/v) 180 °C 24 h	spindle-shaped particles (500 nm)	C-coating (sucrose) post-annealing (650 °C, 5 h, Ar)	CR2025 coin cell	75:15:10 wt% (LCP/C: Super P: PVDF)	1 M $LiPF_6$ in FEC/DMC = 1:4 (v/v)	0.1 C	123 mAh/g

Ref.	**Material**	**Reactants**	**Solvent** ***T*** ***t***	**Morphology (particle size)**	**Remarks on synthesis**	**Cell type**	**Electrode composition**	**Electrolyte**	**C rate (remarks)**	**Discharge capacity, 1st cycle**
c) Supercritical fluid (SCF) synthesis										
9	LCP/C	lithium acetyl acetonate $CoCl_2 \cdot 6 H_2O$ H_3PO_4	ethanol 400 °C 4 min	platelets (5–15 nm × 50–250 nm × 100–200 nm)	Oleylamine surfactant C-coating (PEDOT, MWCNT, wet ball milling) post-annealing (300 °C, 2 h, H_2/Ar)	beaker-type 3 electrode glass cell	83:10:7 wt% (LCP/C: acetylene black:PTFE)	1 M $LiPF_6$ in EC/DEC = 1:1 (v/v)	0.2 C	130 mAh/g
10	LCP/C	$LiCH_3COO \cdot H_2O$ $NH_4CoPO_4 \cdot H_2O$ (from $(NH_4)_3PO_4 \cdot 3 H_2O$)	ethanol 400 °C 2 h	nanosheets (2 nm × 500 nm)	PVP additive liquid-phase exfoliation/ solvothermal HPHT lithiation	coin cell[c]	80:10:10 wt% (LCP/C: MWCNT: PVDF)	1 M $LiPF_6$ in EC/DEC = 1:1 (w/w)	0.2 C	153 mAh/g [d]
11	LCP/C	lithium acetyl acetonate $Co(CH_3COO)_2 \cdot 4 H_2O$ H_3PO_4	ethanol 400 °C 6 min	nanorods (50 nm × 0.5–1 µm)	HMD additive C-coating (sucrose) post-annealing (650 °C, 1 h, Ar)	CR2032 coin cell	80:10:10 wt% (LCP/C: acetylene black: PTFE)	1 M $LiPF_6$ in EC/DMC = 1:1 (v/v)	0.1 C	130 mAh/g
12	LCP	$LiCH_3COO$ $Co(CH_3COO)_2 \cdot 4 H_2O$ H_3PO_4	EG 400 °C 10 min	irregular particles (0.7 µm)	post-annealing (650 °C, 4 h, Ar)	Swagelok cell	80:20 wt% (LCP: Super P)	1 M $LiPF_6$ in EC/DMC = 1:1 (w/w)	0.05 C	14 mAh/g
d) Microwave-assisted hydrothermal (MWHT) synthesis										
13	LCP/C	$LiOH \cdot H_2O$ $CoSO_4 \cdot 7 H_2O$ H_3PO_4	H_2O 230 °C 15 min 600 W	cubes (1–5 µm)	C-coating (glucose) post-annealing (700 °C, 4 h, Ar)	CR2032 coin cell	75:12.5:12.5 wt% (LCP/C:–[c]: TAB)	1 M $LiPF_6$ in EC/DEC = 1:1 (v/v)	0.1 C	52 mAh/g
e) Microwave-assisted solvothermal (MWST) synthesis										
14	LCP	$LiOH \cdot H_2O$ $Co(CH_3COO)_2 \cdot 4 H_2O$ H_3PO_4	TEG 300 °C 15 min 0–600 W	nano-thumblike particles (80 nm × 200 nm)	–	CR2032 coin cell	75:12.5:12.5 wt% (LCP:–[c]: TAB)	1 M $LiPF_6$ in EC/DEC = 1:1 (v/v)	0.1 C	115 mAh/g
14	LCP/C	$LiOH \cdot H_2O$ $Co(CH_3COO)_2 \cdot 4 H_2O$ H_3PO_4	TEG 300 °C 15 min 0–600 W	nano-thumblike particles (80 nm × 200 nm)	MWCNT nano-composite	CR2032 coin cell	75:12.5:12.5 wt% (LCP/C:–[c]: TAB)	1 M $LiPF_6$ in EC/DEC = 1:1 (v/v)	0.1 C	120 mAh/g
15	LCP	$LiOH \cdot H_2O$ $Co(CH_3COO)_2 \cdot 4 H_2O$ H_3PO_4	TEG –[c] 15 min 2000 W	irregular particles (0.2–1 µm)	–	CR2032 coin cell	80:10:10 wt% (LCP: Super C65: PVDF)	1 M $LiPF_6$ in EC/EMC = 1:2 (v/v)	0.1 C (CCCV)	128 mAh/g
16	LCP	$LiOH \cdot H_2O$ $Co(CH_3COO)_2 \cdot 4 H_2O$ H_3PO_4	TEG 260 °C 30 min 800 W	nanorods (200 nm × 1 µm)	–	CR2032 coin cell	70:20:10 wt% (LCP: graphite: PTFE)	1 M $LiPF_6$ in EC/DMC = 1:1 (v/v)	0.1 C	67 mAh/g

[a] All reports, including procedures using additional post heat treatments and conductive carbon coatings to improve the performance, are presented. In case several materials were covered in a report, the best performing sample is listed. Differences regarding the cell design (cell type, electrolyte) and charging protocol (C rate, potential window, CV step, etc.) are highlighted as they affect the electrochemical performance.

[b] abbreviations: BA, benzyl alcohol; CCCV, constant-current, constant-voltage charging; CMC, carboxy methyl cellulose; DEC, dimethyl carbonate; DMC, dimethyl carbonate, EC, ethylene carbonate; EG, ethylene glycol; EMC, ethyl methyl carbonate; FEC, fluoroethylene carbonate; HMD, hexamethylenediamine; HPHT, high-pressure high-temperature; HT, hydrothermal; LCP, lithium cobalt phosphate, $LiCoPO_4$; MWCNT, multi-walled carbon nanotubes; MWST, microwave-assisted solvothermal; PEDOT, poly(3,4-ethylenedioxythiophene); PTFE, poly(tetrafluoroethylene); PVDF, polyvinylidene difluoride; PVP, Poly(*N*-vinylpyrrolidone); SCF, supercritical fluid; ST, solvothermal; TAB, teflonized acetylene black; TEG, tetraethylene glycol.

[c] not specified

[d] The specific capacity values were on the basis of pure LCP rather than of LCP/C (carbon content 4.4 wt%).

2 X-ray powder diffraction data, Rietveld refinements

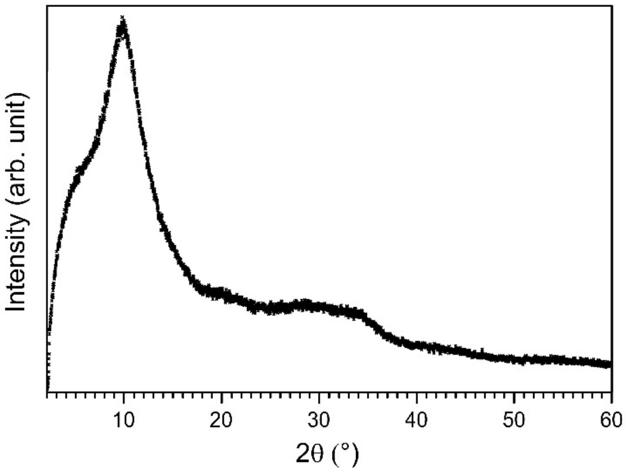

Fig. S1 X-ray diffraction pattern (transmission geometry, Mo $K_{\alpha1}$ radiation, measurement time: 12 h) showing the background profile of an empty borosilicate glass capillary (Hilgenberg, glass type no. 50, length: 80 mm, diameter: 0.5 mm, wall thickness: 0.01 mm). As the maximum intensity of the empty capillary is about 1/10 of the intensity measured when filled with sample, it can be derived that the capillary significantly contributes to the background profile that is observed when the capillary is filled with sample.

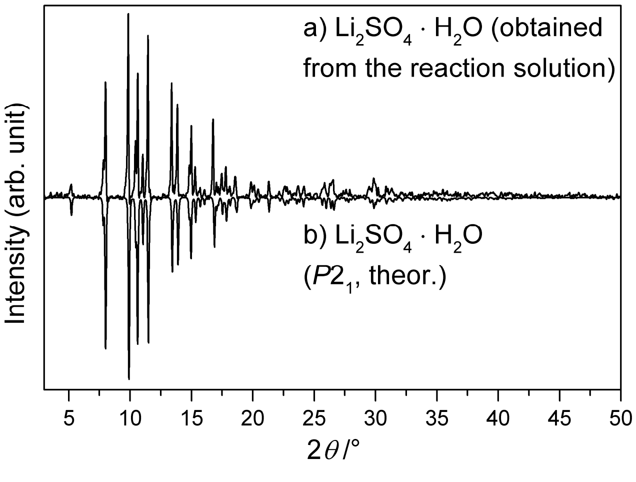

Fig. S2 X-ray powder diffraction pattern (transmission geometry, Mo $K_{\alpha1}$ radiation, measurement time: 20 min) of the white powder obtained from evaporating the reaction solution after the microwave-assisted solvothermal synthesis. The theoretical pattern of $Li_2SO_4 \cdot H_2O$ (ICSD database entry no. 62124) is displayed mirrored in (b). The data confirm that $Li_2SO_4 \cdot H_2O$ was formed as a by-product of the reaction. The powder exhibits comparably low crystallinity, which is also in good agreement with reports that the crystallization of the compound is challenging due to its inverse solubility (i.e., its increasing solubility with decreasing temperature).[17]

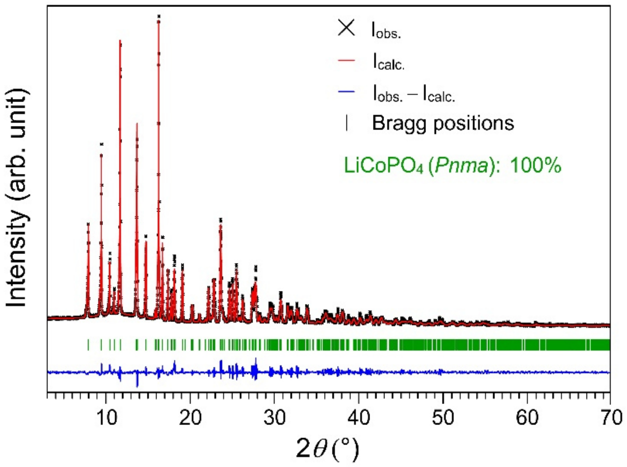

Fig. S3 Rietveld fit of the X-ray powder diffraction data (transmission geometry, Mo $K_{\alpha 1}$ radiation, measurement time: 12 h) of LCP-MW-w obtained from microwave-assisted solvothermal synthesis and after intensive, additional washing with ice water. The diffraction pattern is similar to LCP-MW (Fig. 2 in the main article) and comparable cell parameters can be derived (Table S2b).

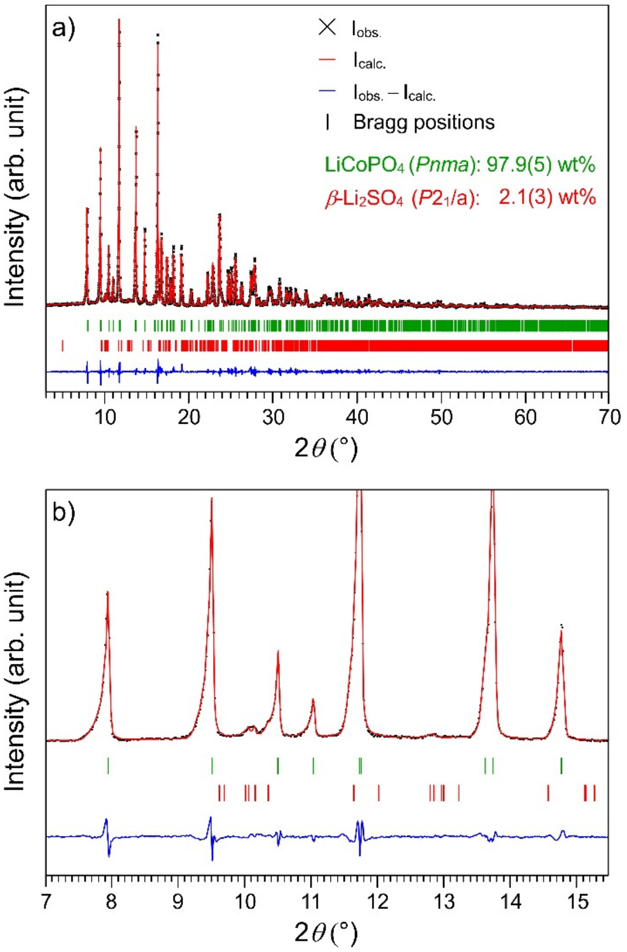

Fig. S4 Rietveld fit of the X-ray powder diffraction data (transmission geometry, Mo $K_{\alpha 1}$ radiation, measurement time: 12 h) of the sample LCP-MW-T obtained after the TGA/DSC measurement under Argon up to 750 °C (see Fig. S5): (a) full pattern, and (b) zoomed view at small 2θ where the peaks of the β-Li_2SO_4 (space group $P2_1/a$) impurity, which crystallizes upon heating, are observed.

Table S2 Refined crystallographic data of $LiCoPO_4$ samples obtained from microwave-assisted solvothermal synthesis: (a) as prepared (LCP-MW), (b) after intensive washing (LCP-MW-w), and (c) after TGA/DSC measurement (LCP-MW-T)[a]

Empirical formula	**a) LCP-MW**	**b) LCP-MW-w**	**c) LCP-MW-T**
M_r (g·mol^{-1})	160.8	160.8	160.8
Crystal system	orthorhombic	orthorhombic	orthorhombic
Space group	*Pnma* (no. 62)	*Pnma* (no. 62)	*Pnma* (no. 62)
Z	4	4	4
a (Å)	10.1930(7)	10.1931(8)	10.1852(9)
b (Å)	5.9188(4)	5.9195(5)	5.9114(5)
c (Å)	4.6959(3)	4.6961(4)	4.6913(4)
V (Å^3)	283.31(3)	283.35(4)	282.46(4)
F(000)	308	308	308
ρ (calcd.) (g·cm^{-3})	3.7710(6)	3.7704(7)	3.7823(8)
T (K)	298	298	298
λ (Å)	0.70930	0.70930	0.70930
R_p	0.0564	0.0633	0.0752
R_{wp}	0.0744	0.0856	0.0996
R_{exp}	0.0550	0.0557	0.0549
R_F	0.0409	0.0331	0.0344
R_B	0.0646	0.0572	0.0575
χ^2	1.35	1.54	1.81
Data/restraints/parameter	4469/0/61	4463/0/61	4469/0/62
Crystalline phase composition	100 wt% $LiCoPO_4$	100 wt% $LiCoPO_4$	97.9(5) wt% $LiCoPO_4$ 2.1(3) wt% Li_2SO_4

[a] The estimated standard deviations (e.s.d's) were calculated by the Berar's procedure und are indicated in parentheses.

Table S3 Fractional atomic coordinates and isotropic thermal displacement parameters refined from X-ray powder diffraction data of $LiCoPO_4$ (*Pnma*, $Z = 4$, $T = 298$ K) samples obtained from microwave-assisted solvothermal synthesis: (a) as prepared (LCP-MW), (b) after intensive washing (LCP-MW-w), and (c) after TGA/DSC measurement (LCP-MW-T)[a]

Sample	**Atom**	**Wyckoff position**	**Occupancy**	***x/a***	***y/b***	***z/c***	**U_{iso} (Å^2)**
a) LCP-MW	Li1	4*a*	1	0	0	0	0.0139[b]
	Co1	4*c*	1	0.2212(2)	¼	0.5210(7)	0.0120(10)
	P1	4*c*	1	0.4046(6)	¼	0.0823(12)	0.0073(16)
	O1	4*c*	1	0.4054(15)	¼	0.766(2)	0.004(2)
	O2	4*c*	1	0.0442(14)	¼	0.292(2)	0.002(2)
	O3	8*d*	1	0.3361(10)	0.0475(14)	0.2160(15)	0.003(2)
b) LCP-MW-w	Li1	4*a*	1	0	0	0	0.0139[b]
	Co1	4*c*	1	0.2214(3)	¼	0.5224(8)	0.0087(12)
	P1	4*c*	1	0.4044(6)	¼	0.0833(13)	0.0036(18)
	O1	4*c*	1	0.4048(17)	¼	0.770(3)	0.003(2)
	O2	4*c*	1	0.0444(16)	¼	0.294(3)	0.003(2)
	O3	8*d*	1	0.3365(11)	0.0485(16)	0.2160(17)	0.003(2)
c) LCP-MW-T	Li1	4*a*	1	0	0	0	0.0139[b]
	Co1	4*c*	1	0.2212(3)	¼	0.5202(9)	0.0085(12)
	P1	4*c*	1	0.4047(7)	¼	0.0827(14)	0.007(2)
	O1	4*c*	1	0.4052(18)	¼	0.758(3)	0.006(2)
	O2	4*c*	1	0.0436(16)	¼	0.295(3)	0.002(2)
	O3	8*d*	1	0.3341(12)	0.0465(17)	0.2147(18)	0.004(2)

[a] The estimated standard deviations (e.s.d's) were calculated by means of the Berar's procedure und are indicated in parentheses.

[b] The Li displacement factor has been fixed in all cases because it cannot be deduced properly by means of X-ray diffraction due to the low atomic scattering factor.

Table S4 Selected interatomic distances refined from X-ray powder diffraction data of $LiCoPO_4$ (*Pnma*, *Z* = 4, *T* = 298 K) samples obtained from microwave-assisted solvothermal synthesis: (a) as prepared (LCP-MW), (b) after intensive washing (LCP-MW-w), and (c) after TGA/DSC measurement (LCP-MW-T)[a]

Atom pair			***d* (Å)**		
			a) LCP-MW	b) LCP-MW-w	c) LCP-MW-T
Li1	O1	×2	2.162(9)	2.178(11)	2.141(12)
	O2	×2	2.068(8)	2.073(9)	2.074(9)
	O3	×2	2.157(9)	2.154(10)	2.173(11)
Co1	O1	×1	2.201(14)	2.202(16)	2.181(18)
	O2	×1	2.100(13)	2.099(15)	2.093(16)
	O3	×2	2.069(9)	2.073(10)	2.055(10)
	O3	×2	2.205(9)	2.206(10)	2.196(11)
P1	O1	×1	1.488(13)	1.470(15)	1.523(16)
	O2	×1	1.540(15)	1.540(17)	1.527(18)
	O3	×2	1.523(9)	1.514(11)	1.532(11)

[a] The estimated standard deviations (e.s.d's) were calculated by applying the Berar's correction und are indicated in parentheses.

3 Thermal stability of LCP-MW

Experimental details

The thermal stability of the single-phase material LCP-MW up to 750 °C was assessed by thermal analysis on a simultaneous TGA/DSC 1 STAR system (Mettler Toledo). Experiments were run at a heating rate of 10 °C/min in an argon stream (10 mL/min, specimen weight: 5 mg). Monitoring of the cooling cycle was not possible due to the setup. The sample that was treated thermally is denoted LCP-MW-T in the following.

In addition to the TGA/DSC experiments, the thermal stability was further examined by temperature-controlled *in situ* PXRD studies using a PANalytical X'Pert Pro diffractometer with monochromatized Cu K_α radiation and an XCelerator detector. The instrument was equipped with an Anton Paar HTK-1200 hot stage, a TCU 1000N temperature controller, and a corundum flat plate sample holder. The scans were collected between 20° and 26° 2θ in Bragg-Brentano geometry (step size: 0.022°, time/step: 1000 s, total measurement time: 76 h). The samples were heated in air at a rate of 5 °C/min, and the patterns collected in a temperature range of 30–900 °C with an increment step of 100 °C, each temperature being held for 5 min before starting the data collection.

Results and discussion

The thermal behavior of the sample LCP-MW was assessed by TGA/DSC and complementary temperature-dependent *in situ* PXRD hot-stage measurements. The TGA/DSC data of the heating cycle are presented in Fig. S5a, the corresponding PXRD data of the sample after the TGA/DSC measurement are presented in Fig. S4. The material is found to be thermally stable up to 750 °C and shows an overall mass loss of only 0.7 wt%, which in agreement with literature.[16, 18] The zoomed view (Fig. S5b) shows an endothermic event at 590 °C that can only be attributed to the reconstructive phase transformation from monoclinic β-Li_2SO_4 (space group $P2_1/a$) to cubic α-Li_2SO_4 (space group $Fm\overline{3}m$)[19-23] and is accompanied by a mass loss of ~0.35 wt%. Moreover, a mass loss of ~0.1 wt% at a temperature of 70–250 °C, and of ~0.2 wt% from 390 °C to 460 °C is observed; both events are not correlated with DSC signals. The observed mass loss might be attributed to the removal of entrained residual water remaining from the synthesis, and the dehydration of traces of the $Li_2SO_4 \cdot H_2O$ impurity.[24, 25] Although these signals show only a low intensity, they are most likely originating from the $Li_2SO_4 \cdot H_2O/Li_2SO_4$ phase.

The PXRD data of the sample LCP-MW-T after TGA/DSC (Fig. S4a) support this observation. Here, traces of crystalline Li_2SO_4 are observed. The refinement of the diffraction pattern delivers a phase fraction of 2.1(3) wt% for the low-temperature phase β-Li_2SO_4 (space group $P2_1/a$).[23] The zoomed view (Fig. S4b) clearly shows the main diffraction peaks of the phase at 10.1° and 12.8° 2θ, respectively. The refined fraction of Li_2SO_4 (2.1(3) wt%, *cf.* Table S2c) is smaller than the one estimated by elemental analysis (5(1) wt%, *cf.* Table 1), which is due to the limitations of the Rietveld method (fractions are not accurately determined if phases show different particle sizes and crystallinities) and the fact that the intensity of the main peaks is comparably small. However, it can be inferred that >94(2) wt% of the sample are the pure LCP phase.

The results as well as the reduction of the amorphous peak at small angles in the PXRD pattern indicate that the lithium sulfate impurity is obtained in amorphous form from the MWST synthesis and can be crystallized upon heating. This is in good agreement with reports that the crystallization of the compound is challenging due to its inverse solubility.[17] Besides that, the LCP phase also seems to increase in crystallinity upon thermal treatment, as it can be derived by the significantly smaller cell volume of about 282.46(4) $Å^3$ (Table S2c). Further details on the refined data of the sample LCP-MW-T can be found in Tables S2, S3, and S4.

In addition to the TGA/DSC experiments, temperature-controlled PXRD studies were carried out to systematically investigate the behavior of LCP-MW upon heating *in situ*. The powder diffraction patterns in a temperature range of 30–900 °C (step size: 100 °C) are displayed in Fig. S6. The focus was set on the 2θ range of 20–26°, the region in which reflections of the $Li_2SO_4 \cdot H_2O/Li_2SO_4$ side phase are expected. In agreement with the TGA/DSC data, no phase changes are observed between 30 °C and 600 °C. Here, the main peaks of the olivine phase (101), (210), (011), and (111) as well as a small reflection that is deriving from the corundum flat plate sample holder at ~24.7° are observed. Signals originating from the lithium sulfate hydrate impurity and its dehydrated form are not detected. This is in agreement with a report[26] that upon dehydration of $Li_2SO_4 \cdot H_2O$, an amorphous unstable anhydride phase is formed. Due to thermal expansion, the $LiCoPO_4$ peaks are continually broadening and shifted to lower angles, indicating bigger lattice dimensions. At 700 °C, a peak around 21.8° is emerging, which can be attributed to the (111) reflection of high-temperature α-Li_2SO_4 (space group $Fm\overline{3}m$)[23] The fact that the phase transition occurs at slightly higher temperatures compared to the DSC might be due to the different atmospheres used for the measurements (air vs. argon), the different heating rates (10 °C/min vs. 5 °C/min), and thermal losses. At a nominal temperature of 900 °C, which is above the melting point of Li_2SO_4,[27] it is possible that the real temperature reached in this experiment was below the melting point due to thermal losses. Therefore, the (111) peak of α-Li_2SO_4 is still visible. Besides, an additional reflection at ~22.1° 2θ is observed. In agreement with current investigations in our group, the peak corresponds to the characteristic (210) reflection of the metastable $Pna2_1$-polymorph of $LiCoPO_4$,[28] which, in contrast to any previous reports about the thermal behavior of olivine-type LCP,[16, 18] is formed at high temperature.

The cooled sample (25 °C) has significantly broader peaks than the initial sample (30 °C) and the reflections are shifted to higher 2θ values due to thermal contraction. According to the reversible phase transformation from β-Li_2SO_4 to α-Li_2SO_4,[19] peaks of low-temperature β-Li_2SO_4 are indicated, which is also consistent with our ex situ PXRD study (Fig. S4). Moreover, reflections of $Li_2SO_4 \cdot H_2O$ arise at 21.6°, 23.0° (shoulder of (210) reflection of LCP), and 25.1° 2θ. The hydrate is formed from the reaction of the hygroscopic Li_2SO_4 with air moisture[29] during the cooling process. The results of the temperature-dependent PXRD study demonstrate and confirm our assumption that the $Li_2SO_4 \cdot H_2O/Li_2SO_4$ secondary phase in the as-obtained LCP-MW product is amorphous and can be crystallized upon heating.

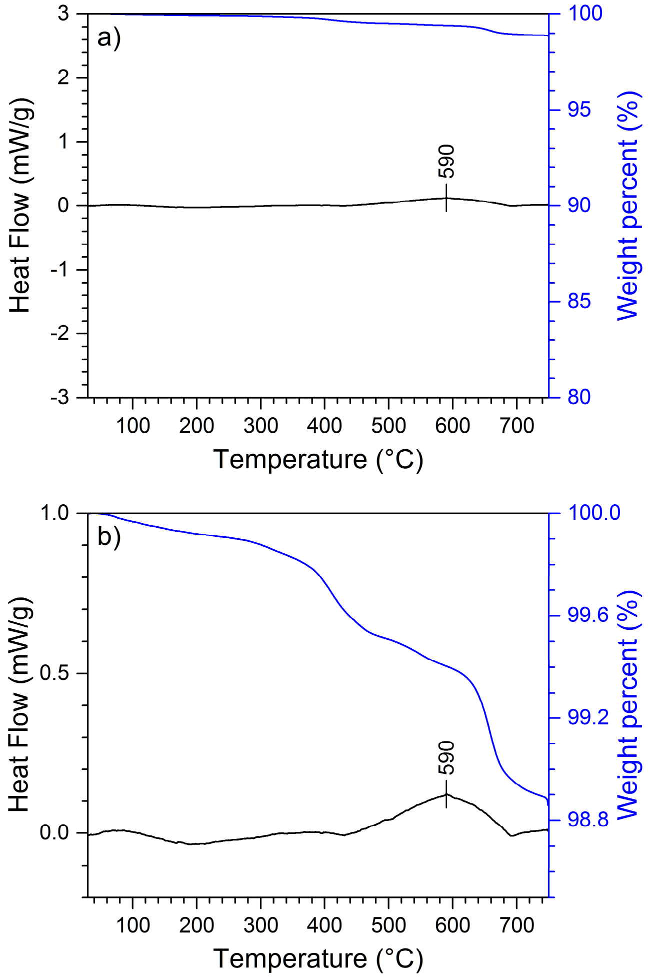

Fig. S5 (a) DSC and TGA plots for the as-prepared material LCP-MW, (b) zoomed view to clarify the weak signals. DSC data are drawn in black, and TGA data in blue.

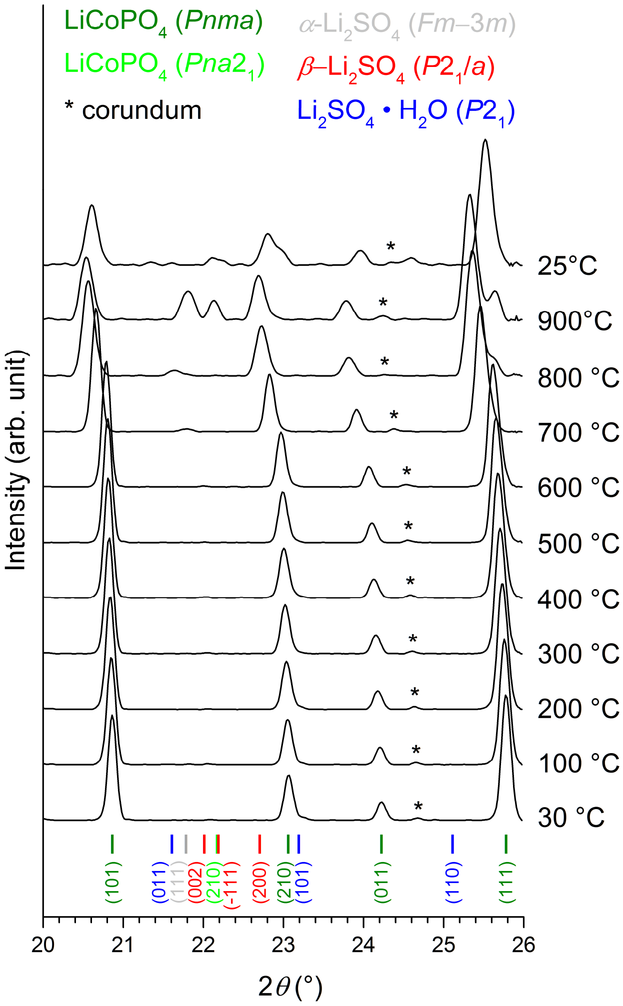

Fig. S6 Temperature-controlled *in situ* X-ray powder diffraction patterns (Bragg-Brentano geometry, Cu $K_{\alpha 1}$ radiation) of the sample LCP-MW in comparison to the main Bragg reflections of the phases $LiCoPO_4$ (*Pnma*, dark green), $LiCoPO_4$ (*Pna*2_1, light green), α-Li_2SO_4 ($Fm\bar{3}m$, red), β-Li_2SO_4 ($P2_1/a$, red), and $Li_2SO_4 \cdot H_2O$ ($P2_1$, blue) from 20° to 26° 2θ. Signals arising from the corundum flat plate sample holder are marked with *.

4 Infrared and Raman spectroscopy

Experimental details

ATR-FTIR spectra were recorded on a Perkin Elmer FTIR spectrometer (diamond ATR, Spectrum Two; located inside an argon-filled glovebox) in a range of 400–4000 cm^{-1}.

Raman spectra were measured by using a Labram HR 800 spectrometer. The instrument was equipped with a 800 mm focal length spectrograph and a cooled (–70 °C), back-thinned CCD detector (pixel size 26×26 μm). The samples were excited by an air-cooled doubled Nd:YAG laser (532 nm), and several input laser powers of 0.056, 0.56, and 5.6 mW were applied. No sample decomposition was observed at any excitation power.

Results and discussion

The FTIR and Raman spectra of LCP-MW are presented in Fig. S7 and the observed vibrations are summed up in Table S5. The IR spectrum is displayed in the full region from 400 cm^{-1} to 4000 cm^{-1} (Fig. S7a) and also in the region of 400–1600 cm^{-1} (Fig. S7b) for clarity. The spectrum does not show any absorption bands of water or other impurities and is in good agreement with reported values.[6, 30-33] In general, it is dominated by the four fundamental intramolecular vibrations of the $[PO_4]$ groups. The bands at 1145 cm^{-1}, 1098 cm^{-1}, and 1044 cm^{-1} are associated with the asymmetric stretching vibrations of P–O (ν_3), which is split up in a triplet due to interactions with the Co–O bonds. The strong singlet at 975 cm^{-1} corresponds to the symmetric stretching vibration of the P–O bond (ν_1). All the observed bonds are broadened, which is a result of the asymmetric bonding situation in the $[PO_4]$ units in the olivine crystal structure. The asymmetry is well confirmed by the refined bond lengths (Table S4a). The triplet observed at 549–640 cm^{-1} is related to antisymmetric bending vibrations of O–P–O (ν_4). The signal at 576 cm^{-1} is related to asymmetric vibrations of the octahedral $[CoO_6]$ units[31] and therefore confirms the olivine structure. The absorption at 471 cm^{-1} can be explained by the symmetric bending vibration of O–P–O (ν_2) or a contribution of Li ion “cage modes”, which represent translational vibrations of the Li ions inside a potential caused by the neighbor oxygen atoms, as discussed in the literature.[34] Due to splitting effects, these bands are overlapping with the phosphate bending vibrations, and an unambiguous assignment cannot therefore be made.

In the IR spectrum, no bands are observed that could be assigned to the lithium sulfate impurity. As it can be derived from the IR spectrum of a mixture of Li_2SO_4 and $Li_2SO_4 \cdot H_2O$ (Fig. S8c,d), the main absorption of the impurity overlaps with one of the ν_3 modes of the P–O vibrations in $LiCoPO_4$. Moreover, it is notable that the IR spectrum remains unaltered for the intensively washed sample LCP-MW-w (Fig. S8a,b).

In the Raman spectrum (Fig. S7c,d), four stretching bands are observed at 1132 cm^{-1}, 1063 cm^{-1}, 977 cm^{-1}, and 938 cm^{-1}, which are in excellent agreement with data reported previously.[34-36] The latter very sharp band is attributed to the intramolecular symmetric stretching vibrations (ν_1) of the $[PO_4]^{3-}$ anion, whereas the two weaker ones are correlated with the asymmetric stretching modes (ν_3). The bending modes of the phosphate group are observed at lower energy. The bands observed at 655 cm^{-1}, 622 cm^{-1}, and 578 cm^{-1} arise from symmetric bending modes (ν_4) while the one at 437 cm^{-1} is from the asymmetric ν_2 mode.[35, 36] Other minor bands have been assigned by the use of density functional theory simulations.[37] The absence of any carbon D or G bands confirms the results of the CHNS analysis that did not detect any carbon in the sample. Moreover, signals that could be attributed to the lithium sulfate secondary phase (i.e. modes of the $[SO_4]^{2-}$ anion) are not detected as expected, because Raman spectroscopy generally provides a lower sensitivity compared to IR.

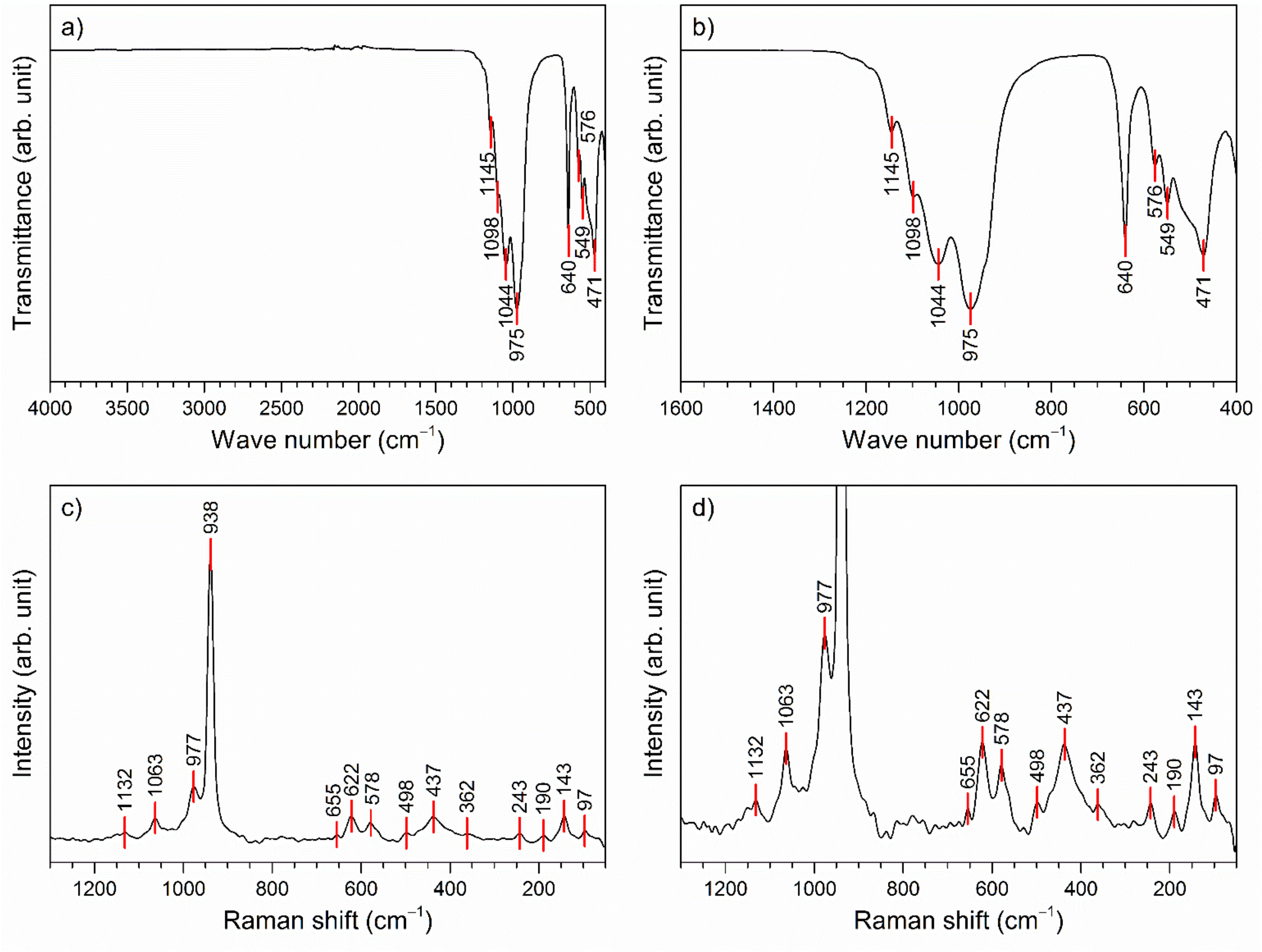

Fig. S7 (a) Full FTIR, (b) zoomed FTIR, (c) Raman, and (d) zoomed Raman spectra of LCP-MW. The sample does not contain any detectable amounts of water or carbon**.**

Table S5 Assignments of the most important (a) IR and (b) Raman bands of LCP-MW as observed in the IR and Raman spectra.[30-32, 34-37]

Vibrational mode		a) FTIR	b) Raman
Asymmetric stretching vibrations of P–O	ν_3	1145 cm^{-1} 1098 cm^{-1} 1044 cm^{-1}	1132 cm^{-1} 1063 cm^{-1} 977 cm^{-1}
Symmetric stretching vibrations of P–O	ν_1	975 cm^{-1}	938 cm^{-1}
Asymmetric bending vibrations of O–P–O	ν_4	640 cm^{-1} 576 cm^{-1} 549 cm^{-1}	655 cm^{-1} 622 cm^{-1} 578 cm^{-1}
Symmetric bending vibration of O–P–O	ν_2	471 cm^{-1}	437 cm^{-1}

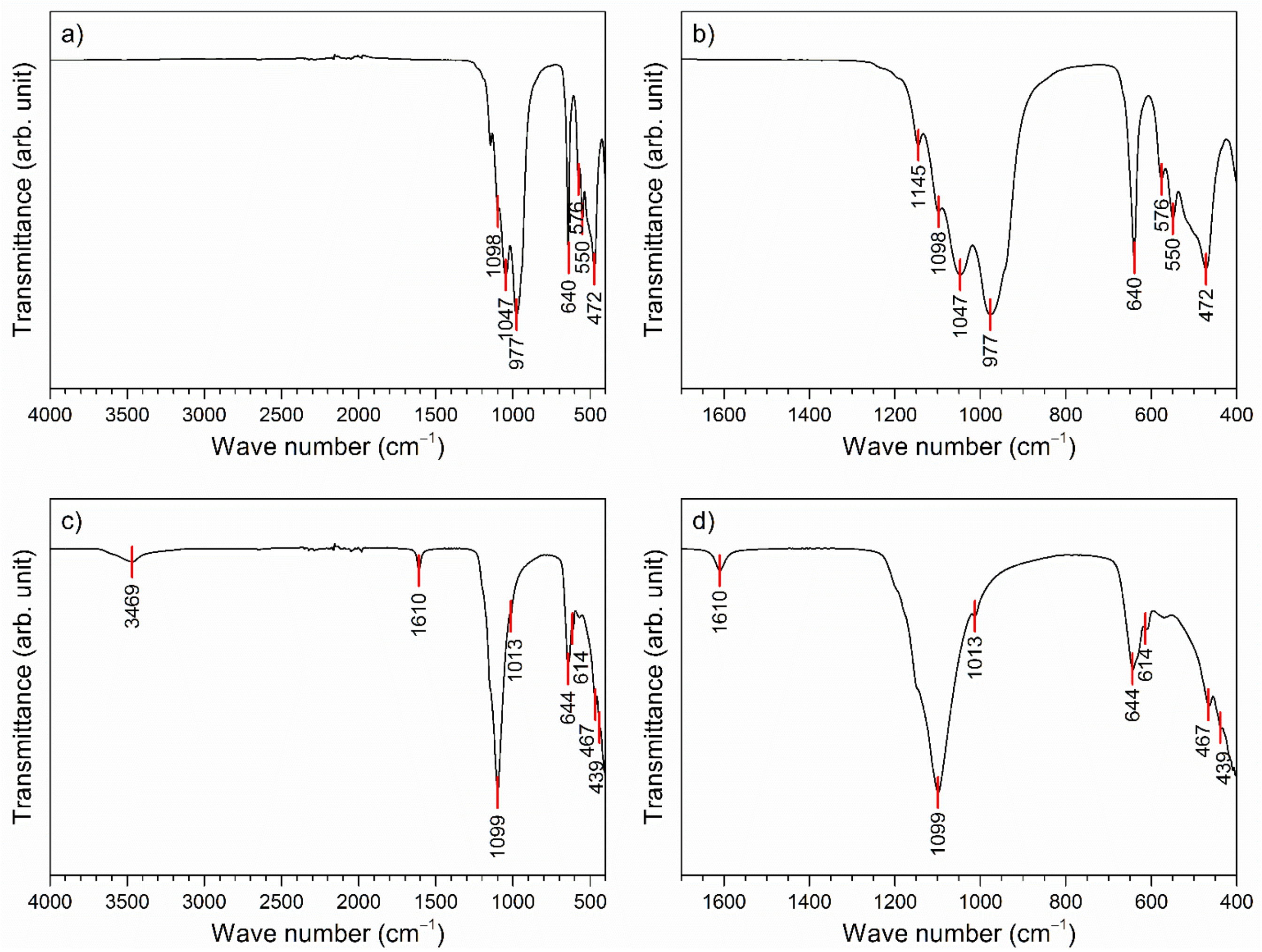

Fig. S8 Full and zoomed FTIR spectra of (a,b) LCP-MW-w (after intensive washing) and (c,d) a mixture of Li_2SO_4 and $Li_2SO_4 \cdot H_2O$.

5 Additional scanning electron microscopy images

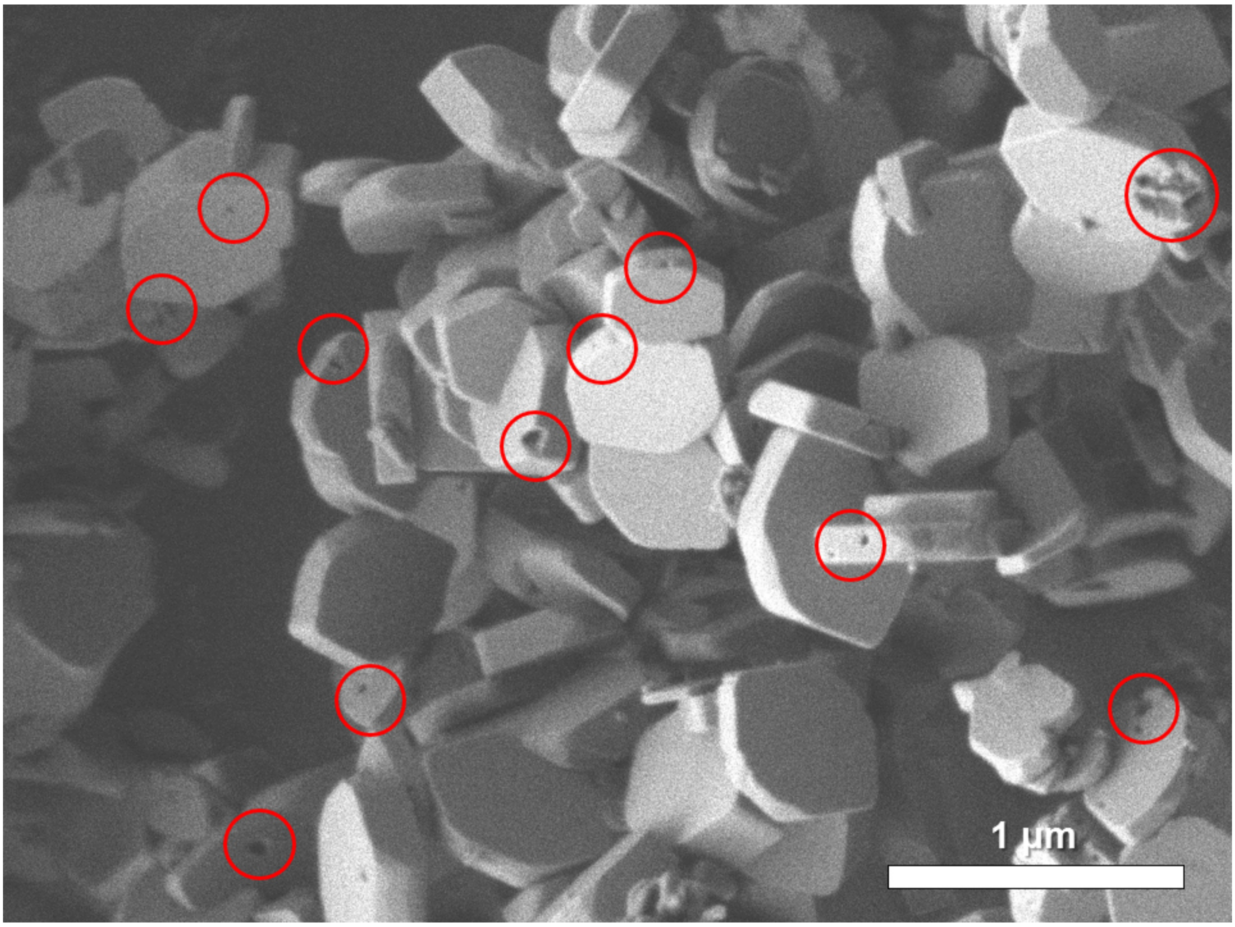

Fig. S9 SEM image of the sample LCP-MW (*cf.* Fig. 3b) showing small pores (diameter: 10–20 nm) on the surface of the particles (indicated by red circles). The pores, which might form an interconnected system, destabilize the particles, with some particles showing damage probably due to mechanical stress during the synthesis produced by stirring and the washing step.

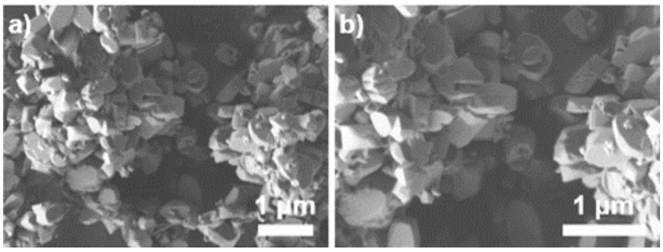

Fig. S10 SEM images of the sample LCP-MW-w (after intensive washing) at two different magnifications (a,b). It can be inferred that increased washing results in a higher portion of damaged particles.

6 Additional electrochemical measurements

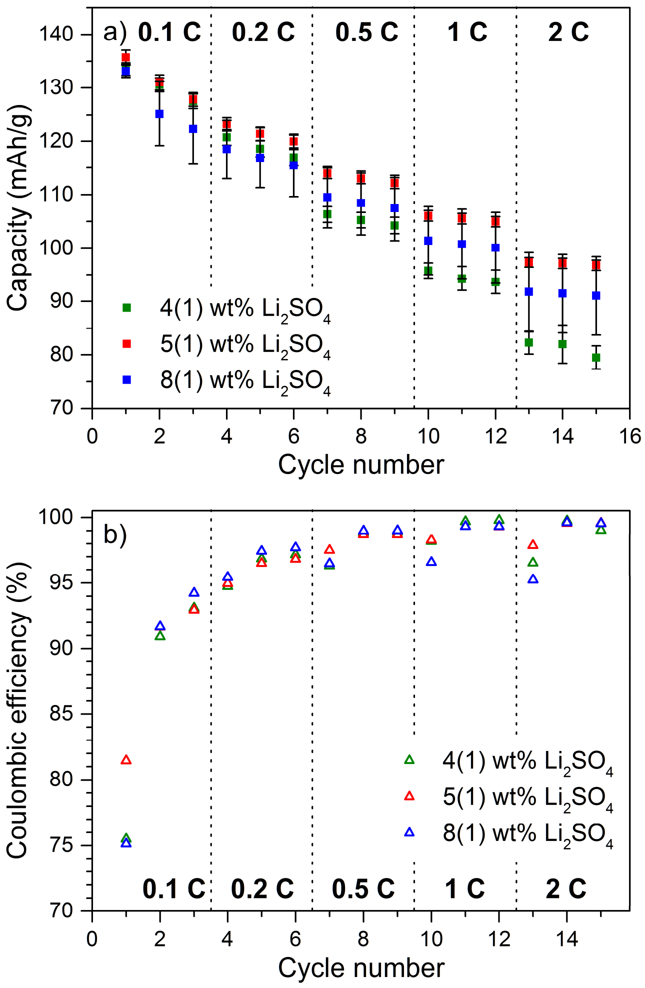

Fig. S11 (a) Specific capacities vs. C rate and (b) coulombic efficiencies (standard deviations omitted for clarity) obtained in each cycle for LCP-MW samples with different quantities of the lithium sulfate impurity. It can be inferred that the Li_2SO_4 content does not affect the electrochemical performance within standard deviations.

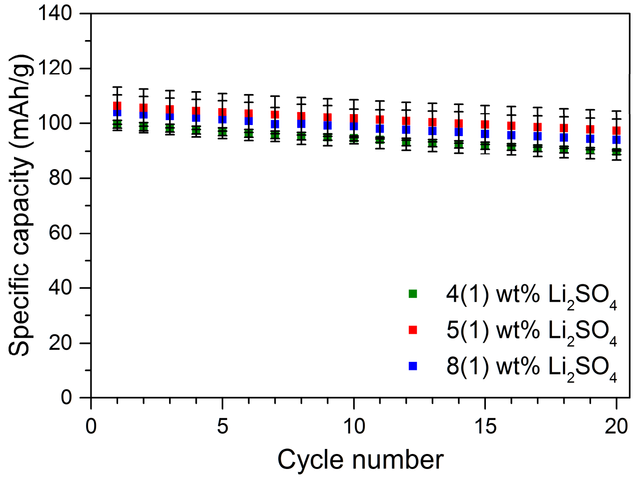

Fig. S12 Comparison of the electrochemical stabilities of LCP-MW MW samples with different quantities of the lithium sulfate impurity at 0.5 C after the first 15 cycles of C rate testing. It can be inferred that the Li_2SO_4 content does not affect the electrochemical stability within standard deviations.

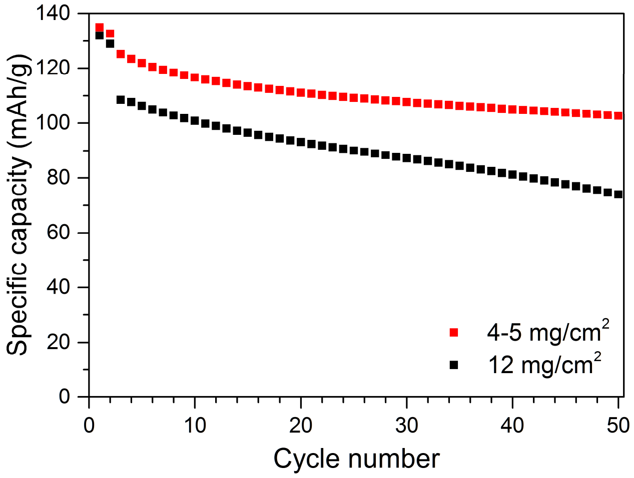

Fig. S13 Comparison of the electrochemical stabilities of LCP-MW electrodes with different loadings of 4–5 mg/cm^2 and 12 mg/cm^2. Testing was performed in Swagelok cells using electrodes with an 80:10:10 wt% composition ratio at 0.5 C after two initial cycles at C/15. It can be inferred that electrodes with high loadings still present reasonable capacities.

References

1 Y. Zhao, S. Wang, C. Zhao and D. Xia, *Rare Met. (Beijing, China)*, 2009, **28**, 117-121.
2 M. Kotobuki, Y. Mizuno, H. Munakata and K. Kanamura, *Phosphorus Res. Bull.*, 2010, **24**, 12-15.
3 F. Wang, J. Yang, Y. Nuli and J. Wang, *J. Power Sources*, 2011, **196**, 4806-4810.
4 M. Kotobuki, *Int. J. Energy Environ. Eng.*, 2013, **4**, 25, 27 pp.
5 M. Li, *Ionics*, 2012, **18**, 507-512.
6 S. Brutti, J. Manzi, A. De Bonis, D. Di Lecce, F. Vitucci, A. Paolone, F. Trequattrini and S. Panero, *Mater. Lett.*, 2015, **145**, 324-327.
7 J. Manzi, M. Curcio and S. Brutti, *Nanomaterials*, 2015, **5**, 2212-2230.
8 B. Wu, H. Xu, D. Mu, L. Shi, B. Jiang, L. Gai, L. Wang, Q. Liu, L. Ben and F. Wu, *J. Power Sources*, 2016, **304**, 181-188.
9 M. K. Devaraju, D. Rangappa and I. Honma, *Electrochim. Acta*, 2012, **85**, 548-553.
10 X. Rui, X. Zhao, Z. Lu, H. Tan, D. Sim, H. H. Hng, R. Yazami, T. M. Lim and Q. Yan, *ACS Nano*, 2013, **7**, 5637-5646.
11 Q. D. Truong, M. K. Devaraju, Y. Ganbe, T. Tomai and I. Honma, *Sci. Rep.*, 2014, **4**, 3975/1-3975/8.
12 M. Kaus, I. Issac, R. Heinzmann, S. Doyle, S. Mangold, H. Hahn, V. S. K. Chakravadhanula, C. Kuebel, H. Ehrenberg and S. Indris, *J. Phys. Chem. C*, 2014, **118**, 17279-17290.
13 A. V. Murugan, T. Muraliganth and A. Manthiram, *J. Electrochem. Soc.*, 2009, **156**, A79-A83.
14 A. V. Murugan, T. Muraliganth, P. J. Ferreira and A. Manthiram, *Inorg. Chem.*, 2009, **48**, 946-952.
15 R. E. Rogers, G. M. Clarke, O. N. Matthew, M. J. Ganter, R. A. DiLeo, J. W. Staub, M. W. Forney and B. J. Landi, *J. Appl. Electrochem.*, 2013, **43**, 271-278.
16 K. J. Kreder, G. Assat and A. Manthiram, *Chem. Mater.*, 2015, **27**, 5543-5549.
17 A. Silambarasan, E. N. Rao, S. V. Rao, P. Rajesh and P. Ramasamy, *CrystEngComm*, 2016, **18**, 2072-2080.
18 J. Chen, M. J. Vacchio, S. Wang, N. Chernova, P. Y. Zavalij and M. S. Whittingham, *Solid State Ionics*, 2008, **178**, 1676-1693.
19 F. D. Rossini, D. D. Wagman, W. H. Evans, S. Levine and I. Jaffe, *Natl. Bur. Stand. Circ. (U. S.)*, 1952, **No. 500**, 1266 pp.
20 T. Forland and J. Krogh-Moe, *Acta Chem. Scand.*, 1957, **11**, 565-567.
21 A. G. Nord, *Crystal structure of the low temperature modification of lithium sulfate (α-Li_2SO_4). Three dimensional refinement*, Univ. Stockholm, 1973.
22 N. W. Alcock, D. A. Evans and H. D. B. Jenkins, *Acta Crystallogr., Sect. B*, 1973, **29**, 360-361.
23 L. Nilsson, J. O. Thomas and B. C. Tofield, *J. Phys. C*, 1980, **13**, 6441-6451.
24 H. Tanaka, *Thermochim. Acta*, 1982, **52**, 195-199.
25 F. Valdivieso, V. Bouineau, M. Pijolat and M. Soustelle, *Solid State Ionics*, 1997, **101-103**, 1299-1303.
26 Y. Seto, H. Sato and Y. Masuda, *Thermochim. Acta*, 2002, **388**, 21-25.
27 G. Hatem and M. Gaune-Escard, *Calorim. Anal. Therm.*, 1983, **14**, 96-103.
28 C. Jaehne, C. Neef, C. Koo, H.-P. Meyer and R. Klingeler, *J. Mater. Chem. A*, 2013, **1**, 2856-2862.
29 R. Weintraub, A. Apelblat and A. Tamir, *Anal. Chim. Acta*, 1984, **166**, 325-327.
30 D. Shanmukaraj and R. Murugan, *Ionics*, 2004, **10**, 88-92.
31 Gangulibabu, D. Bhuvaneswari, N. Kalaiselvi, N. Jayaprakash and P. Periasamy, *J. Sol-Gel Sci. Technol.*, 2009, **49**, 137-144.
32 P. N. Poovizhi and S. Selladurai, *Ionics*, 2011, **17**, 13-19.
33 J. Su, B.-Q. Wei, J.-P. Rong, W.-Y. Yin, Z.-X. Ye, X.-Q. Tian, L. Ren, M.-H. Cao and C.-W. Hu, *J. Solid State Chem.*, 2011, **184**, 2909-2919.
34 C. M. Burba and R. Frech, *J. Electrochem. Soc.*, 2004, **151**, A1032-A1038.
35 W. Paraguassu, P. T. C. Freire, V. Lemos, S. M. Lala, L. A. Montoro and J. M. Rosolen, *J. Raman Spectrosc.*, 2005, **36**, 213-220.
36 E. Markevich, R. Sharabi, O. Haik, V. Borgel, G. Salitra, D. Aurbach, G. Semrau, M. A. Schmidt, N. Schall and C. Stinner, *J. Power Sources*, 2011, **196**, 6433-6439.
37 V. I. Fomin, V. P. Gnezdilov, V. S. Kumosov, A. V. Peschanskii, V. V. Eremenko, S. Gentil and J. P. Rivera, *Low Temp. Phys.*, 1999, **25**, 829-832.